



CO and soot oxidation activity of doped ceria: Influence of dopants



Deboshree Mukherjee, Bolla Govinda Rao, Benjaram M. Reddy*

Inorganic and Physical Chemistry Division, CSIR-Indian Institute of Chemical Technology, Uppal Road, Hyderabad – 500 607, India

ARTICLE INFO

Article history:

Received 23 November 2015

Received in revised form 18 February 2016

Accepted 18 March 2016

Available online 19 March 2016

Keywords:

Doped CeO₂

Dopant influence

Oxygen vacancy

CO oxidation

Soot oxidation

ABSTRACT

This article represents a comparative study of a series of doped ceria catalysts towards environmental applications like CO and soot oxidation catalysis. Transition and rare earth metals of varying size and reducibility property have been selected namely, zirconium (Zr), hafnium (Hf), iron (Fe), manganese (Mn), praseodymium (Pr), and lanthanum (La) as dopants. A facile coprecipitation approach has been used to incorporate the dopants into ceria lattice. The formation of homogeneous solid solutions and their respective physicochemical properties have been confirmed by employing XRD analysis, BET surface area measurements, TEM, Raman, UV-DRS, XPS, and TPR techniques. All the doped CeO₂ samples exhibited smaller crystallite size, larger BET surface area, and higher amounts of oxygen vacancies than that of pure CeO₂. CO oxidation has been performed in the presence of oxygen under atmospheric pressure, and 300–850 K temperature range in a fixed bed microreactor. Soot oxidation was carried out in presence of air using a thermo gravimetric analyzer within a much wider temperature window of 300–1273 K. The physicochemical properties of the doped ceria materials have been comparatively analyzed to correlate the influence of dopants with their improved behaviour in both the oxidation reactions. Vital role of 'lattice oxygen' in CO oxidation and 'active oxygen species' in soot oxidation on the catalyst surface has been considered, assuming that Mars and van Krevelen mechanism and active oxygen mechanism play the key role in CO and soot oxidation, respectively. The O 1s XP spectra confirmed that Mn doped ceria (denoted as CM) exhibited most loosely bound lattice oxygen and highest concentration of surface adsorbed oxygen species compared to other materials. Accordingly, a superior CO and soot oxidation activity have been observed for manganese doped ceria. Significant lowering of T₅₀ (390 K and 669 K for CO and soot oxidation respectively) temperature have been observed in both the oxidation reactions; which is primarily attributed to the considerable lowering of lattice oxygen binding energy and higher concentration of surface adsorbed oxygen species.

© 2016 Elsevier B.V. All rights reserved.

1. Introduction

Designing advanced doped ceria (CeO₂) materials has drawn immense research interest due to their extensive use in several environmental, energy related, and other industrial catalytic applications [1]. The importance of CeO₂ had primarily emerged from its oxygen storage capacity (OSC) and redox catalytic property [2]. Easy toggling between the oxidation states of cerium ion (Ce³⁺/Ce⁴⁺) accompanied with the formation of internal oxygen vacancies imparts excellent redox property in ceria [3]. Moreover, compared to bulk, nanoscale ceria shows outstanding catalytic activity in many applications, which is attributed to an increased specific surface area and relative ease of oxygen vacancy formation than that of the bulk material [4]. Despite its wide advantage, pure ceria

lacks some important features necessary for commercial applications. Low OSC, significant loss of active surface area due to thermal sintering, deactivation of the redox couple, reduction of catalytic activity are few among them [5–7]. Even a small degree of sintering causes a huge effect on the crystallite size and the existence of oxygen vacancies, enough to carve down the catalytic activity significantly [8]. However, presence of a foreign metal ion in the ceria lattice is well proven to strengthen its hand against thermal sintering and loss of catalytic activity, along with significant increase of OSC [9]. In addition, incorporation of dopants results in enhanced BET surface area and oxygen vacancies; thereby, reasonably improve catalytic performance even at higher temperatures [10].

The choice of a suitable dopant however, still remains a major challenge to the scientific community in terms of oxygen storage capacity, thermal stability, and economical considerations. Numerous attempts have been performed to correlate the influence of dopant features, such as oxidation state, ionic radius, electroneg-

* Corresponding author.

E-mail addresses: bmreddy@iict.res.in, mreddy@yaho.com (B.M. Reddy).

activity, etc with the physicochemical properties and redox ability of ceria-based catalysts both from theoretical understanding and experimental observations. To mention a few, Nolan has correlated the ionic radii of trivalent dopants with the kind of defect formed on CeO_2 (110) surface from DFT+U calculations [11]. Hu et al. have illustrated the variation in oxygen vacancy formation energy in terms of valance of dopant ion from theoretical calculations [12]. Anderson et al. have correlated redox catalytic efficiency of doped material with the dopant ionic radius applying DFT calculations [13]. On the other hand, Liu et al. have illustrated a linear correlation between CO oxidation activities of doped ceria with Pauling electronegativity of the dopants from experimental observation [14]. Further, Sun et al. have demonstrated size dependent OSC of ceria nanocrystals after carrying out an in-depth analysis [15]. But combining the outcomes of those studies towards better understanding of the influence of dopant features is not straight forward. Therefore, still there exists a gap at the bottom.

Considering this fact, we have focused particularly on the correlation of physicochemical properties of doped ceria catalysts with their catalytic activity in CO and soot oxidations, which are typically performed in ceria based automobile catalysts [16–20]. CO and soot are generated due to partial burn of fossil fuel in auto mobile engine and exhibit severe effects on environment and human health [21–25]. Therefore, abatement of CO and soot has been a big concern throughout. Ceria based catalysts have been highly explored for this application from 1980s. Number of doped ceria materials have been reported to exhibit considerable activity. Lack of appropriate substitute of fossil fuel and progressively tightened emission standards have provoked more interest in this area [26–28]. Though a plenty of doped ceria catalysts are already reported to exhibit considerable activity, but their comparative study is necessary towards basic understanding of influence of dopants, which have not been well explored yet. To achieve this perception we have undertaken this comparative study and have discussed the outcomes on the basis of present observations and previous literature reports. Catalytic materials have been prepared using different class of dopant metal ions with widely varied ionic radii and reducibility, such as, zirconium (Zr), hafnium (Hf), iron (Fe), manganese (Mn), lanthanum (La), and praseodymium (Pr). Transition metals Zr and Hf have comparatively smaller ionic radii than Ce and are hardly reducible under the redox condition of ceria [20]. They are known to exist in +4 oxidation state and are capable of introducing only intrinsic oxygen vacancies. On the other hand, Mn and Fe are even smaller in size and easily reducible [7,10]. They are known to exist in multiple valance state and thereby impart extrinsic oxygen vacancy along with the intrinsic oxygen vacancies present in ceria. On the contrary, rare earth lanthanum (La) and praseodymium (Pr) exhibit higher ionic radii than Ce but Pr is easily reducible and exhibit in multiple valance state in contrary to La [19,23]. However, both of these metal ions introduce extrinsic oxygen vacancies in addition to intrinsic oxygen vacancies. Moreover, according to literature reports, La modifies the surface property of ceria which leads to formation of comparatively stable surface carbonates [19,20]. Hence, here it will be interesting to comparatively study those doped ceria materials together and analyze their physicochemical properties with their activity.

The catalysts have been prepared by choosing optimized Ce/M ($M = \text{Zr, Hf, La, Pr, Fe, Mn}$) mole ratio according to our previous investigations [20,29–31]. All the catalysts have been prepared via simple facile coprecipitation method under similar laboratory conditions to exclude any difference in activity caused by morphology. All the prepared materials have been calcined at 773 K and characterized using state of art techniques like X-ray diffraction (XRD), transmission electron microscopy (TEM), Raman, UV–vis diffuse reflectance spectroscopy (UV–vis DRS), X-ray photoelectronspectroscopy (XPS). Reducibility of the prepared materials has

been investigated using temperature programmed reduction (TPR). Activity has been studied by performing CO oxidation in presence of oxygen under atmospheric pressure, 300–850 K temperature range and soot oxidation in presence of air in thermogravimetric analyzer within 300–1273 K temperature range.

2. Experimental

2.1. Catalyst preparation

The optimized solid solutions of $\text{CeO}_2\text{-ZrO}_2$ (CZ, 8:2), $\text{CeO}_2\text{-La}_2\text{O}_3$ (CL, 8:2), $\text{CeO}_2\text{-Pr}_2\text{O}_3$ (CP, 8:2), $\text{CeO}_2\text{-HfO}_2$ (CH, 8:2), $\text{CeO}_2\text{-Fe}_2\text{O}_3$ (CF, 9:1) and $\text{CeO}_2\text{-Mn}_2\text{O}_3$ (CM, 8:2) were synthesized by means of simple and economical coprecipitation method. The employed metal precursors were $\text{Ce}(\text{NO}_3)_3 \cdot 6\text{H}_2\text{O}$ (Sigma Aldrich, AR grade), $\text{Zr}(\text{NO}_3)_4 \cdot 5\text{H}_2\text{O}$ (Fluka, AR grade), $\text{La}(\text{NO}_3)_3 \cdot 6\text{H}_2\text{O}$ (Sigma Aldrich, AR grade), $\text{Pr}(\text{NO}_3)_3 \cdot 6\text{H}_2\text{O}$ (Sigma Aldrich, AR grade), HfCl_4 (Sigma Aldrich, AR grade), $\text{Fe}(\text{NO}_3)_3 \cdot 9\text{H}_2\text{O}$ (Sigma Aldrich, AR grade) and $\text{Mn}(\text{NO}_3)_2 \cdot 4\text{H}_2\text{O}$ (Sigma Aldrich, AR grade) respectively. In a typical experimental procedure the requisite quantities of respective metal precursors were dissolved in distilled water separately and mixed together under efficient stirring condition. Dilute aqueous NH_3 was added as precipitating agent in drop wise manner to the above mentioned solution under vigorous stirring until it reached appropriate pH of ~ 9 . Afterwards, the solution was kept under stirring condition for 24 h at room temperature. The resultant precipitate was filtered off and washed several times with double distilled water, until it was free from the anionic impurities. The obtained precipitate was allowed to dry at 373 K for 12 h in electrical oven and the obtained cake was crushed in ceramic mortar in order to get fine powder. Finally, the resultant powder was calcined at 773 K for 5 h in air atmosphere at a heating of 5 K min^{-1} to obtain the final solid solution. For comparison purpose we have also prepared pure ceria by similar procedure.

2.2. Catalyst characterization

Structural features of the prepared catalysts were studied with the help of XRD technique. XRD patterns were recorded on a Rigaku diffractometer using $\text{Cu K}\alpha$ radiation (0.1540 nm), operated at 40 kV and 40 mA in the 2θ range of $2\text{--}80^\circ$ with a 2θ step size of 0.02° and a time for step of 2 s. The XRD phases present in the synthesized samples were identified with the help of Powder Diffraction File-International Centre for Diffraction Data (PDF-ICDD). The average crystallite size and lattice parameters of the prepared samples were estimated using full width at half maximum (FWHM) of the most prominent X-ray diffraction peak by means of Debye-Scherrer equation.

The textural properties such as surface area, pore volume, and pore size distribution of synthesized samples are determined by N_2 adsorption-desorption isotherms which are obtained using Micromeritics ASAP 2010 instrument. Prior to the analysis, the samples were evacuated at 423 K for 12 h to remove the residual moisture and flushed with argon gas for 2 h.

The transmission electron microscopy and high resolution transmission microscopy (TEM-HRTEM) studies were made on a TECNAIG2TEM microscope equipped with a slow-scan CCD camera and at an accelerating voltage of 200 kV. For the TEM analysis, few milligrams of the samples were taken and dispersed in ethyl alcohol. Further, the sample was subjected for ultra-sonication until the samples were completely dispersed in ethanol solution. After well dispersion, a droplet was deposited on a copper grid supporting a perforated carbon film and allowed to dry. The specimen was examined under vacuum at room temperature.

Raman spectra of the samples were recorded on a Horiba Jobin-Yvon HR800 Raman spectrometer equipped with a liquid-nitrogen cooled charge coupled device (CCD) detector and a confocal microscope. The emission line at 632.81 nm from an Ar⁺ ion laser was focused on the sample under microscope and the obtained wavenumbers are accurate to within 1 cm⁻¹ range.

The UV–vis DRS measurements were performed over the wavelength range 200–800 nm using a GBS-Cintra 10e UV–vis NIR spectrophotometer with an integration sphere diffuse reflectance attachment. Samples were diluted in a KBr matrix by pelletization. The XPS studies of the synthesized catalysts were performed using a Thermo K-5 Alpha XPS instrument at a pressure higher than 1×10^{-9} torr. The X-ray source utilized was Mg K α (1253.6 eV) radiation. The core level binding energies (BEs) were charge corrected with respect to the adventitious carbon (C 1s) peak at 284.8 eV.

Temperature programmed reduction (TPR) analysis was undertaken for evaluating the reduction properties of prepared catalysts using an automated Micromeritics AutoChem II-2720 instrument equipped with a thermal conductivity detector (TCD). Approximately 40 mg of the sample was taken and placed in the middle of U-shaped quartz reactor (Inner diameter 5 mm) with the help of quartz wool. Before the TPR analysis, the sample was pre-heated at a rate of 10 K min⁻¹ to 473 K by passing pure He gas at a flow rate of 30 ml min⁻¹ for 30 min over the catalyst to clean the surface of the catalysts. After that, the temperature of the reactor was cooled down to room temperature, and then the reducing agent i.e. 5 vol% H₂/Ar was introduced with a flow rate of 20 ml min⁻¹. Afterwards, the temperature was programmatically raised to 1073 K at a ramp of 5 K min⁻¹, keeping all other parameters unchanged. The outlet of the reactor was connected to a cold trap to absorb the water molecules resulted by the reduction of the catalysts.

2.3. Catalytic activity assessment

2.3.1. CO oxidation

The catalytic activity of the as prepared ceria solid solutions was evaluated for oxidation of CO at atmospheric pressure and temperatures in the range of 300–773 K in a fixed bed microreactor at a heating ramp of 5 K min⁻¹. About 100 mg of the catalysts, (250–355 μ m sieve fraction) diluted with similar size quartz particles were placed in the middle of the quartz reactor with the help of quartz wool for catalytic evaluation. Temperature was measured directly at the catalyst bed, using a thermocouple placed in the hollow part of the reactor. The flowing gases and gas mixtures utilised (supplied by Air Liquid) were: argon (>99.999% purity), 9.98% CO in argon (CO purity, >99.997%; argon purity, >99.99%), and 10.2% O₂ in argon (oxygen purity, >99.995%). The total flow rates maintained by three mass flow controllers were in the range of 50–60 NmL min⁻¹ (millilitres normalized to 273.15 K and 1 atm). The CO and CO₂ gas concentrations were measured using an Uras 14 infrared analyzer module, and the O₂ concentration was measured using a Magnus 16 analyzer (Hartmann & Braun). Prior to oxidation of CO, the prepared catalysts were heated to 773 K in the presence of 10.2% O₂/Ar gas mixture, using a heating ramp of 10 K min⁻¹, and kept at the final temperature for 1 h. The oxidized samples were then purged in argon and cooled to the desired starting temperature. The CO/O₂ reactant feed ratio was 1, and partial pressures of CO and O₂ were in the range of 10 mbar.

2.3.2. Soot oxidation

The catalysed soot oxidation was carried out in a thermo gravimetric analyzer (Mettler Toledo, TGA/SDTA851e). The soot oxidation experiments were performed by heating the soot and catalyst mixtures at the rate of 10 K min⁻¹ from 300 to 1273 K in 100 ml min⁻¹ flow of air. These experiments were conducted repeatedly for 4–5 cycles using the same sample. No appreciable

change in the soot oxidation efficacy was noticed. The activity measurements were performed in ‘tight contact’ (ground in an agate mortar) condition with catalyst-soot mixtures in 4:1 wt/wt ratio. In this experiment, the model soot used is Printex-U provided by Degussa. This soot was proven to be an appropriate model for the soot oxidation reaction.

3. Results & discussion

3.1. Characterization studies

XRD is a powerful technique to determine the crystal structure and phase purity. The XRD patterns of the prepared catalysts CM, CF, CH, CP, CL, and CZ calcined at 773 K are illustrated in Fig. 1. The diffraction pattern of pure ceria is also provided for the purpose of comparison. A careful observation of Fig. 1 reveals that, XRD patterns of all the prepared doped CeO₂ samples are indexed to (111), (200), (220), (311), (420), and (422) planes, which are characteristic of fluorite like cubic structure of CeO₂ (JCPDS, No. 34-0394), as established in the literature [32,33]. Further, no characteristic peaks pertaining to individual component oxides namely ZrO₂, HfO₂, Pr₂O₃, La₂O₃, Fe₂O₃, and MnO₂ were observed, which signifies incorporation of the dopant ions into the ceria lattice, or the oxides might be present in highly amorphous or well dispersed state, that is beyond instrument's detection limit. Interestingly, the diffraction peaks of doped CeO₂ are broader with 2 θ values shifted to various extents compared to pure CeO₂ (Fig. S1, supporting information). This significant observation indicates the existence of smaller crystallites along with either lattice contraction or expansion depending on the size parity between dopant and cerium ions. The diffraction peaks of CM, CF, CH, and CZ samples were shifted to higher broad angle side, whereas the peaks of CP and CL were shifted to lower angle side compared to pure CeO₂. Shift in the peak positions could be elucidated by comparing the ionic radii of the guest (Mn³⁺ ~ 0.72 Å, Fe³⁺ ~ 0.78 Å, Zr⁴⁺ ~ 0.72 Å, Hf⁴⁺ ~ 0.85 Å, La³⁺ ~ 1.17 Å, and Pr⁴⁺ ~ 1.13 Å) and host ions (Ce⁴⁺ ~ 0.87 Å). Obviously, incorporation of La³⁺ and Pr⁴⁺ with higher ionic radii compared to Ce⁴⁺, led to lattice expansion, resulting in peak shift to lower Bragg's angle, as expected [34]. On the contrary, peak shift to higher Bragg's angle for CM, CF, CH, and CZ is attributed to lattice contraction due to substitution of Ce⁴⁺ by smaller sized Mn³⁺, Fe³⁺, Hf⁴⁺, and Zr⁴⁺

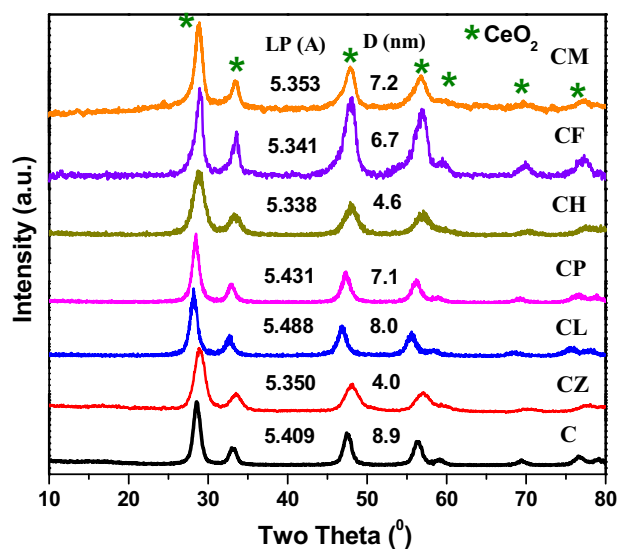


Fig. 1. Powder X-ray diffraction patterns of pure ceria (C), ceria-zirconia (CZ), ceria-lanthana (CL), ceria-praseodymia (CP), ceria-hafnium (CH), ceria-iron (CF) and ceria-manganese (CM) samples calcined at 773 K.

Table 1

Average crystallite size (nm), lattice parameter (°A), BET surface area (m² gm⁻¹), F_{2g} Raman shift (cm⁻¹) and lattice strain (ε) of pure ceria (C), ceria-zirconia (CZ), ceria-lanthana (CL), ceria-praseodymia (CP), ceria-hafnium (CH), ceria-iron (CF) and ceria-manganese (CM) samples calcined at 773 K.

Sample	Crystallite size D (nm) ^a	Lattice parameter a (°A) ^a	Lattice parameter a (°A) ^b	Surface area (m ² gm ⁻¹)	F _{2g} Raman shift (cm ⁻¹) ^c	Lattice strain (ε) ^a
CeO ₂ (C)	8.9	5.409	5.411	41	460.5	0.0053
CeO ₂ -ZrO ₂ (CZ)	4.0	5.350	5.345	84	475.1	0.0250
CeO ₂ -La ₂ O ₃ (CL)	8.0	5.488	5.543	66	447.6	0.0263
CeO ₂ -Pr ₂ O ₃ (CP)	7.1	5.431	5.463	72	455.0	0.0121
CeO ₂ -HfO ₂ (CH)	4.6	5.338	5.402	78	469.4	0.0285
CeO ₂ -Fe ₂ O ₃ (CF)	6.7	5.341	5.392	68	447.8	0.0367
CeO ₂ -Mn ₂ O ₃ (CM)	7.2	5.353	5.384	58	440.5	0.0381

^a From XRD spectra.

^b From Vegard's law.

^c From Raman analysis.

dopant cations [35]. Accordingly, a decrease in the lattice parameter is noticed for CM, CF, CH, and CZ samples in comparison to pure CeO₂, whereas the CP and CL samples showed an increased lattice parameter (Table 1). For comparison, Vegard's law has also been applied to calculate the theoretical lattice parameters. Vegard's law for ceria-based solid solutions is expressed in Eq. (1) [36]:

$$a = 5.411 + \sum (0.0220\Delta r_k + 0.0015\Delta z_k)m_k \quad (1)$$

Where k stands for dopants; the difference between ionic radius of doped element and Ce is obtained from $\Delta r_k = r_k - r_{Ce}$; the valence difference is derived from $\Delta z_k = z_k - z_{Ce}$; m_k signifies the molar percentage of the doped element k; and 5.411 °A is the lattice constant of cubic CeO₂. Interestingly, for CL and CH the experimental values deviate considerably from the theoretical values. Incorporation of larger La³⁺ cation should lead to increase in cell volume; whereas addition of smaller Hf⁴⁺ should produce a decrease in lattice parameter value. Compared to pure CeO₂ larger and smaller values have been observed for CL and CH respectively, as expected. However, the experimental values are smaller than the theoretical values in both the cases, which probably aroused due to the presence of synergistic interaction between the doped elements and Ce⁴⁺ cation [37]. However, the observed key features of the XRD pattern, such as peak shift, variation in the lattice parameter and absence of peaks pertaining to the dopant metal oxides confirmed the formation of ceria solid solutions.

In order to explore the influence of dopants on the textural properties of ceria, average crystallite sizes, and specific surface areas were determined. The obtained values are presented in Table 1. The average crystallite size of the doped CeO₂ samples without considering lattice strain are calculated by taking more intense diffraction peak (111) with the help of Scherer equation ($d = 0.9\lambda/\beta\cos\theta$). Notably, the incorporation of dopants led to a decrease in the crystallite size of ceria, indicating that, formation of Ce-O-M arrested the crystal growth of CeO₂ against higher thermal treatments. However, XRD peak broadening is resulted from size and/or lattice strain which is approximately expressed by Williamson–Hall (W–H) in Eq. (2) [38].

$$\beta\cos\theta/\lambda = 1/D + \eta\sin\theta/\lambda \quad (2)$$

Where, β is the FWHM in radians, λ is the wavelength of X-ray radiation, θ is the Bragg angle of the corresponding peak, D is the effective crystallite size, and η is the effective strain. $\beta\cos\theta/\lambda$ is plotted against $\sin\theta/\lambda$ and the plotted points are linearly fitted. After linear fitting the intercept gives the effective crystallite size (D) and slope (η) gives the strain. The corresponding graphs and the magnitudes of strain (ε) are shown in Fig. S2 (A–G) (supporting information) and in Table 1, respectively. The crystallite sizes obtained from the plots are 10.16, 9.69, 16.949, 13.09, 10.08, 37.31, 30.03 nm for C, CZ, CL, CP, CH, CF, and CM respectively. However, since W–H equation includes many approximations, the values obtained cannot be considered accurate. The size variation of Ce⁴⁺

and Ce³⁺ and the oxygen vacancies create distortion in the local symmetry of ceria and generate lattice strain [39]. Dopants introduce additional lattice strain by means of creation of additional oxygen vacancies. By undergoing lattice expansion, CeO₂ releases the internal strain. Since W–H plot gives the crystallite size with considering strain, so these values are higher than that of the size obtained from Scherer's formula where the strain term is not considered. Higher lattice strain induces higher oxygen mobility, which improves oxidation reaction via Mars and van Krevelen mechanism [40].

N₂-adsorption and desorption studies were undertaken to determine the specific surface area of the doped CeO₂ samples, and the obtained values are summarized in Table 1. In general, the mixed oxides exhibit higher BET surface area in comparison to the individual oxides [41]. As proclaimed, the surface area of CeO₂ was significantly increased after incorporation of dopant metal ions. The specific surface area of C, CM, CL, CF, CP, CH, and CZ samples are 41, 52, 66, 68, 72, 78, and 84 m²/g, respectively, which corroborates well with the crystallite size decrease (Table 1). The obvious correlation between crystallite size and surface area of the prepared materials reveals that Zr⁴⁺ incorporation into the CeO₂ reduced its crystallite size and enhanced its surface area to highest extent compared to others.

Transmission electron microscopy was undertaken to further evaluate the morphology, lattice structure and particle size of the synthesized ceria-based samples. Fig. 2 represents the high resolution TEM images (HRTEM) of the ceria-based samples namely C, CZ, CL, CP, CH, CF, and CM calcined at 773 K. A careful observation of the figure reveals that all samples were present in well crystalline form with uniform distribution and morphology of nanosized particles. The average size of particles are found to be in the range of ~4–10 nm for all samples, which is matched well with crystallite size obtained from XRD analysis. It is clear from the HRTEM images that the lattice fringes for all samples found to be visible with interplanar spacing of about 0.31 nm, which attributed to CeO₂ (111) plane with the XRD peak at 28.6° (Fig. 1). Interestingly, the lattice fringes corresponding to dopant oxides were not observed in HRTEM images. This remarkable observation may be due to the replacement of cerium ions with dopant ions in the ceria lattice resulting in the formation of nanosized Ce–O–M (M = Zr, La, Pr, Hf, Fe and Mn) solid solutions.

Raman scattering provides useful information regarding electronic and phonon structure of materials. The different symmetries involved determine whether the vibrations are Raman active and appear in the spectra; whereas the changes in lattice spacing and chemical environment govern the shifts in band frequencies. CeO₂ with cubic fluorite type structure belongs to the Fm3m space group and exhibits an exceptionally simple vibrational structure with one infrared active phonon of T_{1μ} symmetry and one Raman active phonon of T_{2g} symmetry [42]. This Raman active triply degenerate stretching vibration of CeO₈ vibrational unit manifests in the

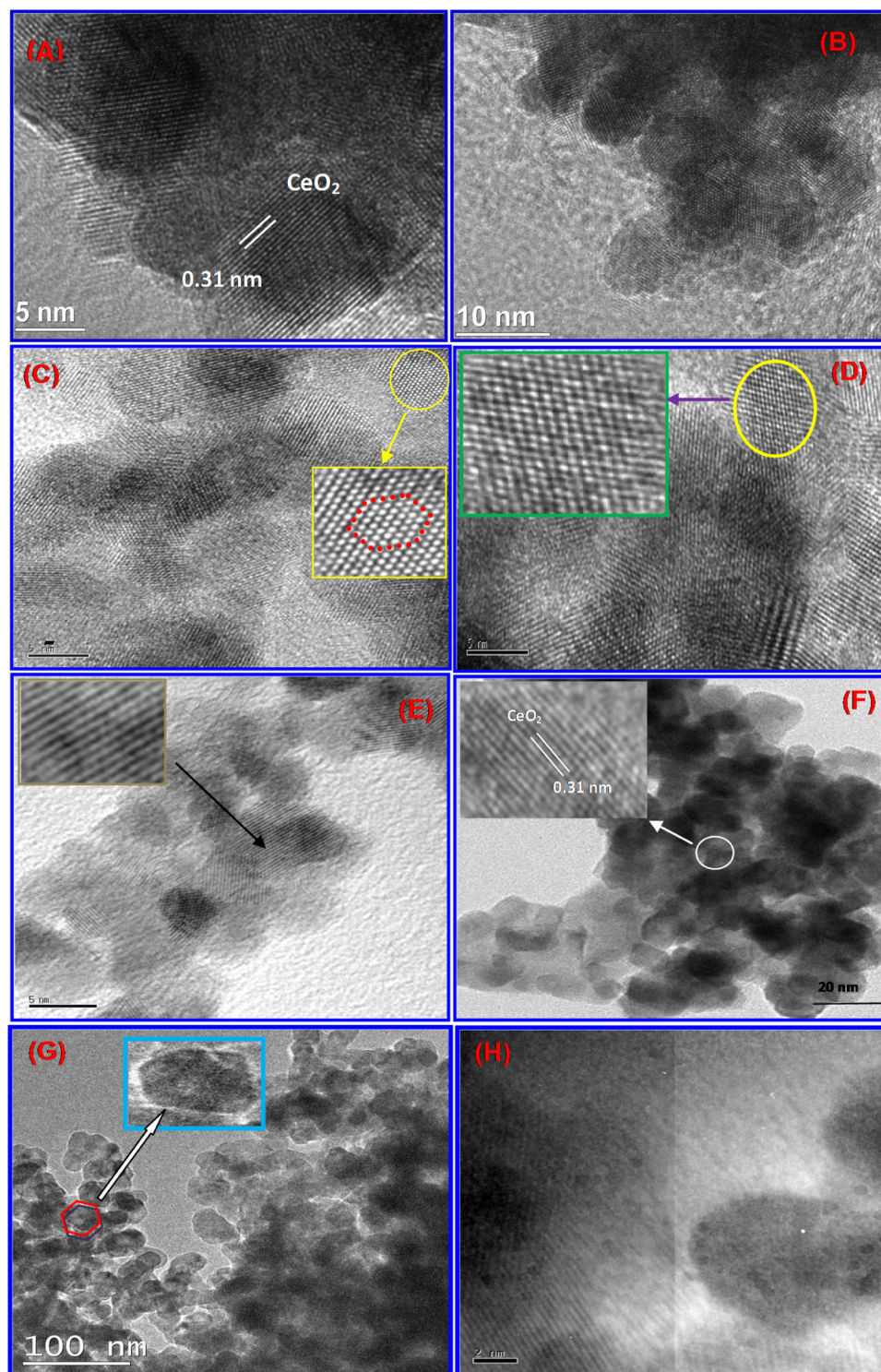


Fig. 2. HREM micrograms of pure ceria (A), ceria-zirconia (B), ceria-lanthana (C), ceria-praseodymia (D), ceria-hafnium (E), ceria-iron (F) and TEM and HREM images of ceria-manganese (G,H) samples calcined at 773 K.

form of a single sharp peak $\sim 465\text{ cm}^{-1}$ and can be attributed to the symmetric breathing mode of oxygen atoms [43]. This renders the vibration very sensitive to microstructural changes such as oxygen sublattice disorder and nonstoichiometry [44]. These changes may also result in the appearance of a broad feature within approximately $550\text{--}600\text{ cm}^{-1}$, which is attributed to the oxygen vacancies [45]. In the present work, Raman spectroscopic study of all the prepared samples has been carried out to explore the microstructures

and oxygen vacancy defect formation in the mixed oxide samples. Fig. 3 represents the Raman spectra of the samples including the pattern of pure CeO_2 for comparison. Notably, the entire mixed oxide samples exhibited a prominent peak with high intensity indicating the F_{2g} peak of CeO_2 . The F_{2g} peak values of the respective samples are furnished in Table 1. No Raman bands corresponding to dopant oxides such as ZrO_2 , HfO_2 , Pr_2O_3 , La_2O_3 , Fe_2O_3 , and Mn_2O_3 were identified in the investigated Raman region, again confirming

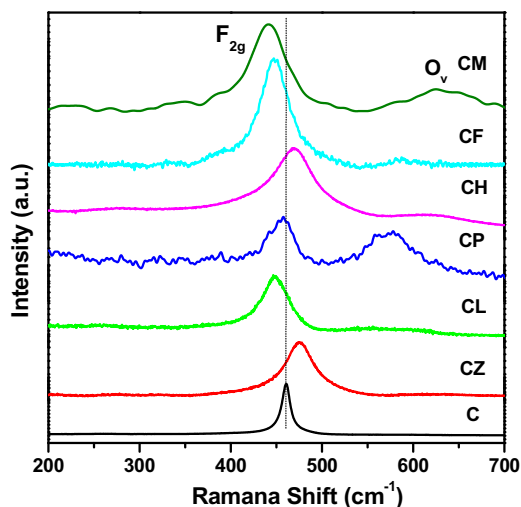


Fig. 3. Raman spectra of pure ceria (C), ceria-zirconia (CZ), ceria-lanthana (CL), ceria-praseodymia (CP), ceria-hafnium (CH), ceria-iron (CF) and ceria-manganese (CM) samples calcined at 773 K.

the formation of ceria-based cubic fluorite solid solutions, as was ascertained from XRD analysis. However, their F_{2g} peak positions (Table 1) have been shifted to different extents depending on the employed dopant. Interestingly, the F_{2g} bands of CZ and CH samples are shifted to higher wavenumber side, whereas the F_{2g} bands of CL, CP, CF, and CM samples are shifted to lower wave numbers relative to pure CeO_2 . The shift in the F_{2g} mode revealed the variation of the M–O vibration frequency, due to the difference in the ionic radii of Ce^{4+} and dopants [46]. Further, all the samples exhibited a broad peak in between 550 to 650 cm^{-1} , which can be attributed to lattice defects, resulting from the formation of oxygen vacancies [47]. As can be noted from Fig. 3, this peak is less prominent in the case of pure CeO_2 , while it became stronger in the mixed oxides and is most noticeable in case of CP and CM samples. This indicates formation of more oxygen vacancies in CP and CM samples to compensate charge imbalance occurred due to presence of aliovalent praseodymium and manganese cations and the resultant increase in Ce^{3+} concentration.

UV–vis DRS is a promising technique to study the oxygen-metal coordination environment and existence of charge transfer bands in nanosized doped ceria materials and other transition metal oxides. This examination provides useful information regarding the changes in bulk, surface coordination, and different oxidation states of the ions by measuring d–d and f–d transitions, and oxygen-metal ion charge transfer bands [48]. Pure ceria (773 K calcined) exhibits three absorption maxima in the UV region centered at ~255, 285, and 340 nm. The former two bands correspond to $\text{Ce}^{3+} \leftarrow \text{O}^{2-}$ and $\text{Ce}^{4+} \leftarrow \text{O}^{2-}$ charge transfer transitions, respectively, and the latter is assigned to interband transitions [49]. However, a careful examination of Fig. 4 revealed that CP sample exhibits one more intense absorption band in the visible region (400–650 nm) which might be associated with Pr^{3+} ion transitions [20]. Further, it can be seen that CM exhibits a distinctive blue-shift of the adsorption edge (interband transition) as compared to ceria. This could be attributed to the presence of Mn^{3+} ions in the system which would cause a significant increase in the Ce^{3+} fraction on the CM surface; thereby resulting in an increase in the charge-transfer gap between the O 2p and Ce 4f orbitals and induced blue shift in the absorption edge [50]. Moreover, the characteristic $\text{Ce}^{3+} \leftarrow \text{O}^{2-}$ charge transfer band appears distinct in the case of CM samples. These results imply the higher concentration of oxygen vacancy defects in the samples corroborating with the Raman spectroscopy studies.

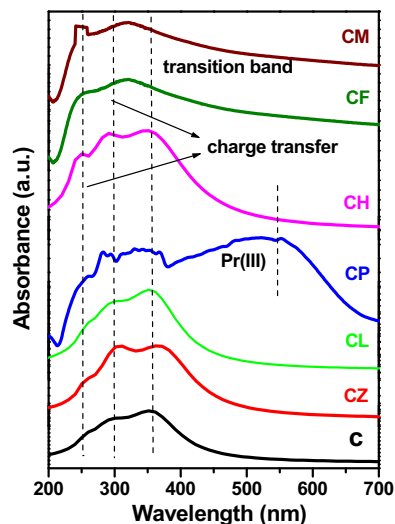


Fig. 4. UV–vis DR spectra of pure ceria (C), ceria-zirconia (CZ), ceria-lanthana (CL), ceria-praseodymia (CP), ceria-hafnium (CH), ceria-iron (CF) and ceria-manganese (CM) samples calcined at 773 K.

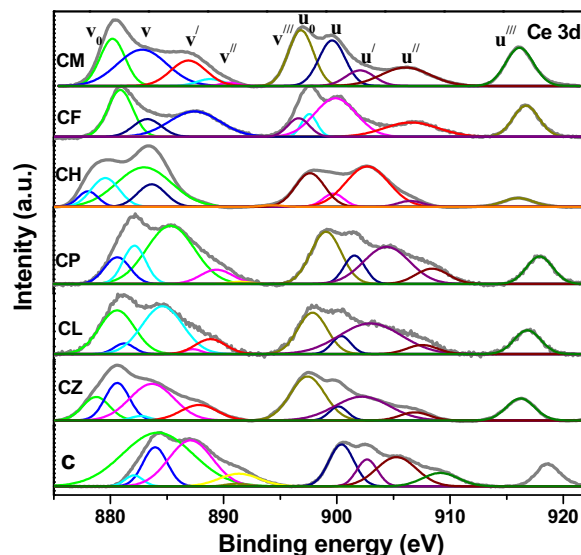


Fig. 5. The deconvoluted Ce 3d core level XP spectra of pure ceria (C), ceria-zirconia (CZ), ceria-lanthana (CL), ceria-praseodymia (CP), ceria-hafnium (CH), ceria-iron (CF) and ceria-manganese (CM) samples calcined at 773 K.

XPS is a powerful surface probe. It furnishes useful information regarding the kind of elements present on the surface and their respective oxidation states. It also allows direct determination of concentration of the identified surface elements. Hence, XP spectra of the Ce 3d core level of the respective samples in the range 880–920 eV have been recorded and presented in Fig. 5. Ce 3d photoelectron peaks displayed a complex nature of spectrum originated from the existence of multiple oxidation states and overlapping of Ce 4f levels with O 2p states during the primary photoemission process. Based on previous literature, the Ce 3d spectrum can be assigned into two sets of spin-orbital multiplets, corresponding to the $3d_{3/2}$ and $3d_{5/2}$ contributions and are labelled as u and v, respectively [20,24]. The peaks labelled v and v' have been assigned to a mixing of $\text{Ce } 3d^9 4f^2 \text{ O } 2p^4$ and $\text{Ce } 3d^9 4f^1 \text{ O } 2p^5$ of Ce^{4+} states, and the peak denoted v'' corresponds to the $\text{Ce } 3d^9 4f^0 \text{ O } 2p^6$ of Ce^{4+} final state. On the other hand, lines v_0 and v' are assigned to $\text{Ce } 3d^9 4f^2 \text{ O } 2p^5$ and $\text{Ce } 3d^9 4f^1 \text{ O } 2p^6$ of Ce^{3+} [20]. The same assignment has also been applied to the u structures, which

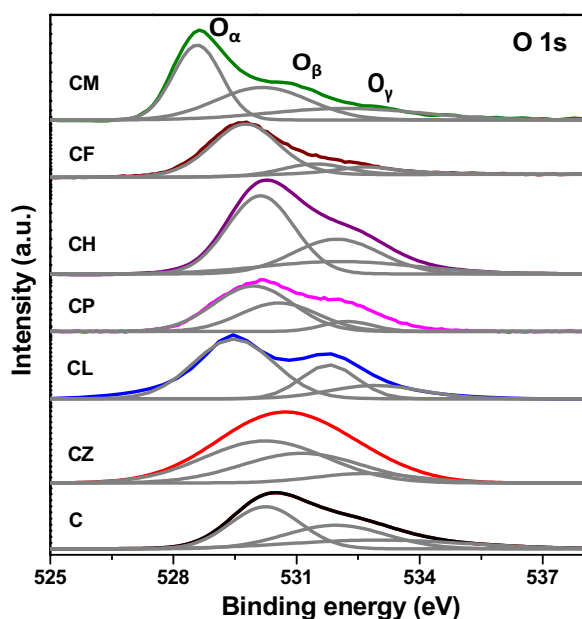


Fig. 6. The deconvoluted O 1s core level XP spectra of pure ceria (C), ceria-zirconia (CZ), ceria-lanthana (CL), ceria-praseodymia (CP), ceria-hafnium (CH), ceria-iron (CF) and ceria-manganese (CM) samples calcined at 773 K.

correspond to Ce 3d_{3/2} levels. As shown in Fig. 5, the XP spectrum of all the samples calcined at 773 K exhibit peaks due to both Ce⁴⁺ and Ce³⁺ ions, thus implying that cerium is present on the surface in both 4+ and 3+ oxidation states [51]. Meticulous examination of the Ce 3d XP spectra reveals that u and u₀ peaks pertaining to Ce³⁺ are relatively more intense in case of CM compared to others. This intriguing observation signifies higher fraction of Ce³⁺ on the CM surface, as was earlier observed from Raman spectroscopy and UV–vis DRS.

The O 1s core level spectra of CZ, CL, CP, CH, CF, and CM samples are illustrated in Fig. 6. The same of pure CeO₂ is also provided for the sake of comparison. It can be observed from the figure that the O 1s spectrum is broad and complicated due to the presence of more than one peak arising from the overlapping contributions of different chemical oxygen species bounded to Ce and other dopant ions in the samples. In order to differentiate these oxygen species, the spectra was resolved with Gaussian-Lorentz model functions and the curve fitted into three peaks. The peak observed around 530.2 eV is attributed to lattice oxygen (O_α); while the non-lattice oxygen are assigned to the peaks observed around 531.9, and 533.5 eV, which include surface adsorbed oxygen (O_β), and hydroxyls, chemisorbed water, carbonates (O_γ), respectively [31]. Surface oxygen also includes superoxide (O₂^{•−}) and peroxide (O₂^{2−}) intermediates, which form on the CeO₂ surface during stepwise incorporation of gas phase oxygen into lattice oxygen. However, the surrounding environment of the lattice oxygen in doped CeO₂ becomes different from that of pure CeO₂ due to difference in the electronegativity of the dopant and cerium. This results in shifting of the peak position to different extents. In the present investigation, O_α peak of CM appears at the lowest binding energy, which signifies the presence of loosely bound lattice oxygen. Binding energies of the lattice oxygen (O_α) in the respective samples increase in the order: CM, CF, CH, CL, CP, and CZ (Fig. 6). Here it is worth mentioning that, lattice oxygen is directly involved in CO oxidation via Mars and van Krevelen mechanism [52]. Henceforth, it will be interesting to find out the correlation between the binding energies of O_α and CO oxidation activity in the later section. On the other hand, in literature many authors have reported the key role of surface adsorbed oxygen in soot oxidation under tight contact

condition [21]. The process of soot oxidation involves active oxygen transfer/spill over from surface to the soot leading to eventual formation of CO or CO₂ [20,53]. A careful examination of the O 1s spectra showed comparatively higher intensity of the O_β (surface adsorbed oxygen) peak for CM. Since, O_β takes part in soot oxidation higher amount of surface oxygen indicate improved soot oxidation activity, which will be discussed in later section [54].

The Zr 3d, La 3d, Pr 3d, Hf 4f, Fe 2p and Mn 2p core level spectra of CZ, CL, CP, CH, CF and CM, respectively are represented in Fig. 7(A–F). It can be noticed from Fig. 7A that, Zr 3d core level spectrum of CZ exhibited spin orbit doublet. The peaks observed at binding energies 182.4 and 184.7 eV are attributed to Zr 3d_{5/2} and Zr 3d_{3/2} contributions respectively. Appearance of these peaks confirmed the presence of Zr in +4 oxidation state. No peaks corresponding to other oxidation states were observed. In case of La 3d, the peaks observed at 834.3 and 838.6 eV; 851 and 855.5 eV correspond to 3d_{5/2} and 3d_{3/2} respectively for CL (Fig. 7B). Splitting was observed due to spin orbit interaction and charge transfer from ligand (O 2p) to the metal (La 4f). The splitting energy, valued at 4.25 eV revealed that La was present in +3 oxidation state, which corroborated well with earlier reports [55]. The Pr 3d core level spectrum, shown in Fig. 7C, consisted of two sets of spin-orbit multiplets at binding energies ~933 and ~953 eV, which are designated to 3d_{5/2} and 3d_{3/2}, contributions respectively. The Pr 3d_{3/2} sublevel possessed complexity due to multiplet effect. In order to understand the oxidation states of praseodymium present in CP samples, we have examined the Pr 3d_{5/2} region. The 3d_{5/2} sublevel consisted of two features corresponding to two possible oxidation states (Pr³⁺ and Pr⁴⁺). The spectra showed a pronounced shoulder at 929.8 and 934.5 eV. According to previous results, we assigned the former to Pr³⁺ and the latter to Pr⁴⁺ [29]. Hence we conclude that, Pr exhibited in both +3 and +4 oxidation states in CP sample, which indicates the easy reducible nature of CP. The Hf 4f core level spectrum of CH (Fig. 7D), consisted of two characteristic peaks observed at 17.2 and 18.6 eV corresponding to Hf 4f_{7/2} and Hf 4f_{5/2}, respectively. The binding energy difference between these two components was found to be 1.4 eV, which is in well agreement with the earlier reports [56]. The Fe 2p spectra (Fig. 7E) exhibited two binding energies at ~711.2 and ~724.2 eV, which are attributed to Fe 2p_{3/2} and Fe 2p_{1/2} respectively. Two weak satellite peaks observed at ~718.7 and ~732.4 eV, confirmed that, Fe existed in both +3 and +2 oxidation states in CF. The deconvoluted XP spectra of Mn 2p in CM sample is presented in Fig. 7F. The Mn 2p spectra consisted of a spin-orbit doublet for Mn 2p_{1/2} and Mn 2p_{3/2} contributions with binding energies ~653.1 and ~642.2 eV, respectively, which indicated the mixed-valence nature of manganese in CM sample. However, the Mn 2p_{3/2} spectra further split into three peaks with binding energy 643.7, 641.7, and 640.4 eV, which are attributed to Mn⁴⁺, Mn³⁺, and Mn²⁺, respectively [10]. This observation clearly indicated that Mn ions displayed multiple oxidation states like +2, +3, and +4 in CM sample. The lower binding energy of CM sample compared to pure MnO_x signifies the strong interaction between manganese and cerium oxide.

H₂-TPR is a simple and useful method to extract information regarding the reduction process involved with an oxide material. Reduction of CeO₂ is generally thought to occur via a stepwise mechanism. Firstly, reduction of the outer most layers of Ce⁴⁺ (surface reduction) takes place around <800 K, then reduction of the inner Ce⁴⁺ layer (bulk reduction) occurs at higher temperatures, approximately at 1050 K. The mechanism, put forward to account for this behavior comprises of three sequential steps: (i) dissociation of chemisorbed hydrogen with formation of OH groups, (ii) formation of anionic vacancies with desorption of water by recombination of H and OH (with concomitant reduction of Ce⁴⁺ to Ce³⁺), and (iii) diffusion of surface anionic vacancies into the bulk [57,58]. However, in contrast to this Aneggi et al. [59] have corre-

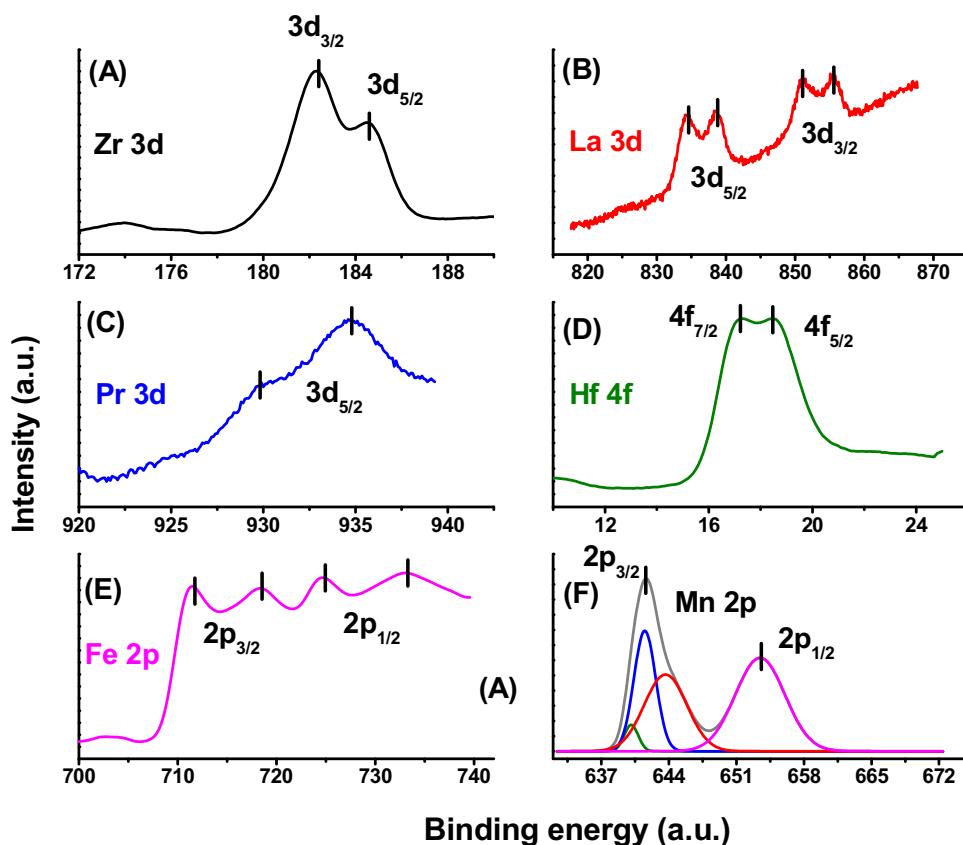


Fig. 7. (A–E) Zr 3d, La 3d, Pr 3d, Hf 4f, Fe 2p and Mn 2p core level XP spectra of ceria-zirconia (CZ), ceria-lanthana (CL), ceria-praseodymia (CP), ceria-hafnium (CH), ceria-iron (CF) and ceria-manganese (CM) samples calcined at 773 K.

lated the bimodal peak of ceria reduction with the different kinetic and thermodynamic properties of nanocrystalline and bulk ceria. Difference in the kinetics and the thermodynamics of reduction of small and large crystallites present in ceria samples are considered to control the reduction pattern [59]. The TPR pattern of all the catalysts has been recorded and the respective TPR profiles are represented in Fig. 8. All the doped samples evidenced low temperature reducibility compared to pure ceria. This facile reducible nature of doped ceria is attributed to the structural modifications in the ceria lattice brought about by the substitution of Ce^{4+} cations with foreign cations, which promotes the diffusion of O^{2-} anions within the lattice [29]. However, Mn remarkably lowered the surface and bulk reduction temperatures of pristine ceria among all the dopants. In the line with earlier literature reports, the lower temperature reduction peak of CM is attributed to reduction of MnO_2 to Mn_3O_4 , and the high-temperature reduction peak was assigned to the reduction of Mn_3O_4 to MnO together with the reduction of surface CeO_2 [60]. It can be assumed that the low temperature reduction pattern of CM had resulted from the synergistic interaction between Mn–O and Ce–O with the formation of CM solid solution, which enhanced the mobility of oxygen species from bulk to the surface, thereby creating more active sites on the surface for adsorption of hydrogen [10].

3.2. Catalytic activity studies

3.2.1. Perspective on CO and soot oxidation

Both the heterogeneous oxidation reactions are very different in terms of working mechanism and the temperature range where the reactions take place. Firstly, to consider with CO oxidation reaction on active metal supported ceria catalyst, two parallel reaction

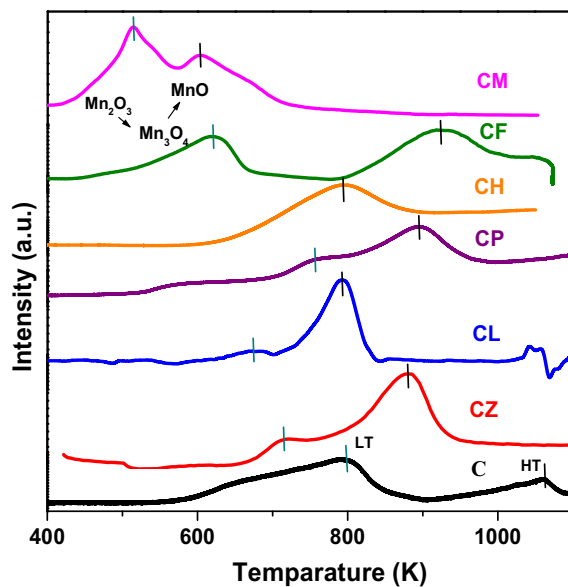


Fig. 8. H_2 consumption profiles of pure ceria (C), ceria-zirconia (CZ), ceria-lanthana (CL), ceria-praseodymia (CP), ceria-hafnium (CH), ceria-iron (CF) and ceria-manganese (CM) samples calcined at 773 K.

mechanisms have been found to prevail the literature [63–65]. One reaction mechanism is Langmuir–Hinshelwood (L–H) mechanism. In this mechanism a CO molecule and an unpaired oxygen atom are attached to adjacent catalyst active sites which then react to form carbon dioxide and released in the atmosphere. Further, oxygen and carbon monoxide molecules from the surrounding atmosphere fill

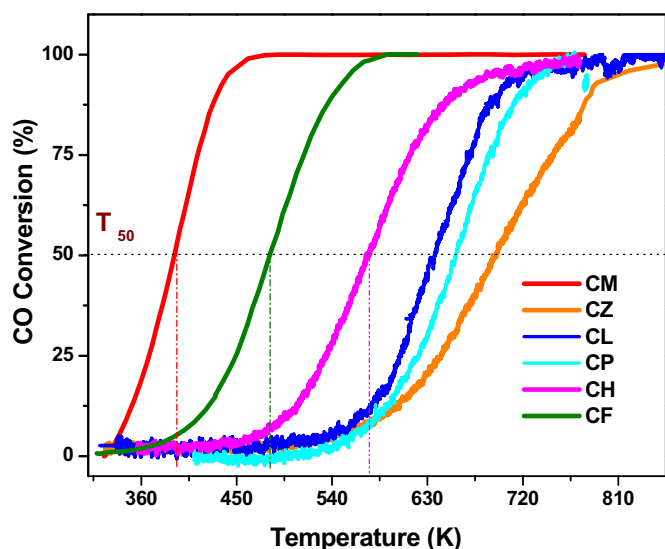


Fig. 9. Conversion of CO over ceria-zirconia (CZ), ceria-lanthana (CL), ceria-praseodymia (CP), ceria-hafnium (CH), ceria-iron (CF) and ceria-manganese (CM) samples calcined at 773 K.

in the voids on the catalyst surface created by the former reactant molecules. The second mechanism for CO oxidation on CeO_2 catalyst is Mars and van Krevelen mechanism. This reaction pathway requires saturation of all the CO adsorption sites on the catalyst surface with carbon monoxide. After attainment of CO saturation condition the oxygen from the ceria surface oxidize the adsorbed CO molecule creating oxygen vacancies which are further filled by the oxygen from surrounding air. However, in real vehicle exhaust where a high CO/low O_2 environment exists the Mars and van Krevelen mechanism is likely to be more favourable [61].

On the other hand in the diesel engine soot is thermally combusted on the diesel particulate filter (DPF) by O_2 and NO_2 present in the vehicle exhaust. Two combustion mechanisms have been identified, which are known as “ NO_2 assisted mechanism” and the “active oxygen mechanism”. In this study soot oxidation has been carried out in absence of NO_2 so active oxygen mechanism probably plays role. According to this pathway in the oxygen rich gas stream of diesel engine exhaust ceria exchanges its oxygen with gas phase oxygen which leads to creation of highly reactive oxygen species, the so called ‘active oxygen’. These highly reactive active oxygen atoms then oxidize soot at soot-ceria interface [62]. The thermal combustion of Diesel soot usually needs temperatures above 450°C , and catalysts play a key role to lower the ignition temperature, hence the stability of the catalytic material at higher temperature range is considered to be of prior importance.

3.2.2. CO oxidation

Carbon monoxide oxidation has been carried out in a fixed bed microreactor under atmospheric pressure and 300–850 K temperature range. The conversion of CO was calculated using the inlet and outlet concentration of CO as per earlier reports [63]. The activity results corresponding to various samples are represented in Fig. 9. As is apparent from the figure, with increasing reaction temperature the CO conversion increased and resulted in sigmoid type curves for all the catalysts, irrespective of doped element. For comparison purpose, we have calculated the temperature at which 50% conversion occurred, mentioned as T_{50} . The T_{50} temperature of CM, CF, CH, CL, CP, and CZ are 390, 480, 573, 635, 655 and 693 K, respectively. As is apparent from the figure, CM exhibits the lowest T_{50} temperature among all, which is followed by CF, CH, CL, CP, and CZ in an ascending order. Here it will be interesting to correlate

the activity order observed to the characteristics of the doped ceria catalysts. The DFT + U studies have demonstrated that CeO_2 (110) plane is the active surface for CO oxidation [64]. In the stepwise process of CO oxidation via Mars and vanKrevelen mechanism, ceria undergoes a redox cycle, in which ceria is reduced by CO at first, and immediately oxidized by gas phase oxygen in the feed gases. The main steps involved in the CO oxidation process are expressed as follows [65,66]:



Here, “*” represents adsorption sites on the surface, and the species with this suffix means the corresponding adsorption species. “ O_L ” and “ V_L ” are denoted as the lattice oxygen and the oxygen vacancies in ceria, respectively. Eq. (3) represents the process of CO adsorption on the ceria surface. These adsorbed CO reacts with the lattice oxygen in the following step with the formation of reaction intermediates (Eq. (4)). Consequent desorption of the reaction intermediates generate CO_2 and oxygen vacancies; hence refresh the adsorption sites (Eq. (5)). In the following step, the gas phase oxygen is activated on the catalyst to replenish the oxygen vacancies (Eq. (6)). Here it should be noted that, formation of carbonate and carboxylate like complexes over CeO_2 surface on exposure to CO atmosphere is also reported in literature [67,68]. In-situ FTIR study of CO adsorption has demonstrated existence of three types of bands for adsorbed CO, including bidentate carbonate, unidentate carbonate and inorganic carboxylate [69,70]. Liu et al. have revealed that the processes involved in Eq. (3), Eq. (5), and Eq. (6) are not the determinant factors of CO oxidation process. Rather, extraction of lattice oxygen, as expressed in Eq. (4) is the rate determining step of the whole process [71]. Obviously, easy availability of the active lattice oxygen and faster oxygen migration from bulk to surface would enhance the CO oxidation activity. However, the overall reactivity is also affected by carbonate formation on the catalyst surface. As mentioned earlier, fraction of CO/ CO_2 slightly accumulates on the catalyst surface forming carbonate like species which hinders further adsorption of fresh CO molecule and retards the reaction rate [59]. The process of accumulation of carbonates mainly depends on the acid/base property of the doped CeO_2 surface [31]. In our earlier study as well in other literature reports we found that La doped ceria is more prone towards carbonate accumulation, which is also reflected in the comparatively lower activity of CL in the present study [31,72,73].

Table 1 show that the CO oxidation activity of the catalysts is not consistent with the magnitude of BET surface area. Among all the modified ceria catalysts, CM manifests highest activity in terms of low temperature CO conversion, in spite of exhibiting the lowest BET surface area. This clearly indicates that the surface area does not control the activity. Therefore, the low temperature CO conversion activity of CO could be attributed to other factors. Most interestingly, the O 1s XP spectra revealed that, the lattice oxygen of CM are much loosely bound compared to other prepared materials. The lattice oxygen binding energies of the prepared materials increased in the order $\text{CM} < \text{CF} < \text{CH} < \text{CL} < \text{CP} < \text{CZ}$. The order perfectly matches with the increasing order of T_{50} temperatures of CO oxidation of the respective catalysts. In literature some authors have proposed involvement of superoxide and peroxide species in CO oxidation, which is however contradictory and the role of molecular oxygen is more likely to heal the oxygen vacancy rather than being involved in a direct reaction with adsorbed CO [74–76]. In the present study the direct correlation between the lattice oxygen binding energy with the activity order further supports this fact. This fascinating

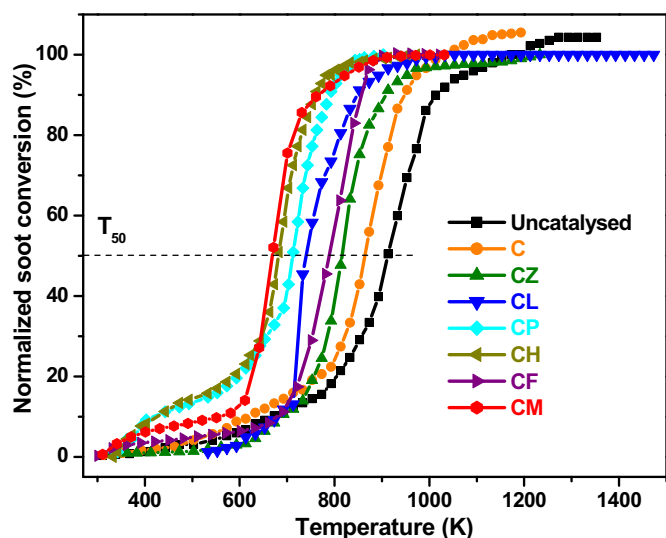


Fig. 10. Normalized soot conversion (%) v/s reaction temperature (K) of uncatalyzed soot, pure ceria (C), ceria-zirconia (CZ), ceria-lanthana (CL), ceria-praseodymia (CP), ceria-hafnium (CH), ceria-iron (CF) and ceria-manganese (CM) samples calcined at 773 K.

observation leads us to infer that, low binding energy of lattice oxygen, which might be attributed to the electronegativity disparity of the host and dopant ions, controls the availability of lattice oxygen and CO oxidation activity of the respective catalysts. Furthermore, the higher degree of lattice strain developed in CM enhanced the mobility of oxygen in the bulk and helped in maintaining the oxygen flow from bulk to surface. To mention the other probable reasons for higher activity of CM, XPS and Raman spectra evidenced highest concentration of Ce^{3+} and higher surface oxygen vacancies for CM, which would evidently promote the oxidation capacity of the material. Anderson et al. have suggested a linear correlation between the ionic radii of dopants and oxygen vacancy formation energy [13]. Small ionic radius dopant lowers the vacancy formation energy, which signifies high reducibility of the doped material. In the same line, we assume that comparatively smaller ionic radius of Mn leads to lowering of the vacancy formation energy, resulting in higher reducibility. Apart from these, Mn XPS displayed presence of multiple oxidation states, which indicates the probable existence of synergism between the $\text{Ce}^{4+}/\text{Ce}^{3+}$ and $\text{Mn}^n/\text{Mn}^{n+1}$ redox pairs in the system. Unambiguously, along with introducing extrinsic oxygen vacancy, synergism between the Mn and Ce redox couple would promote the redox catalytic activity of CM. Therefore, it can be concluded that all those factors together contribute towards enhancement of the redox catalytic activity of CM, resulting in remarkably low temperature CO oxidation activity.

3.2.3. Soot oxidation

Soot oxidation has been performed using air in tight contact condition, employing thermogravimetric analyzer within 300–1273 K temperature range. Conversion of soot over the catalysts is presented in Fig. 10 as a function of temperature. The oxidation profile of bare soot is also provided for comparison. The observed T_{50} temperatures of the catalysts CM, CH, CP, CL, CZ, CF, C mixed with soot are 669, 682, 711, 740, 786, 795 K respectively. This observation indicates, the activity order of the catalyst for soot oxidation is: $\text{CM} > \text{CH} > \text{CP} > \text{CL} > \text{CZ} > \text{CF} > \text{C}$. Shangguan et al. have proposed a mechanism for the catalytic oxidation of carbon, which is valid for many metals and mixed metal oxide type catalysts [77,78]. According to this mechanism, the metal oxide catalysts participate in

redox cycle, in which the metal is repeatedly oxidized and reduced. The following steps are involved in the process:



Where, M_{red} and $\text{M}_{\text{oxd}} - \text{O}_{\text{ads}}$ represent the reduced and oxidized states of the catalyst, respectively. O_{gas} and O_{ads} represent the gaseous O_2 and surface adsorbed oxygen species respectively. C_f denotes a carbon active site or free site on the carbon surface, and SOC represents a surface carbon-oxygen complex. According to this mechanism, the gaseous oxygen is dissociatively adsorbed on the surface of metal oxide catalyst, and the resulting atomic O_{ads} species then attack the reactive free carbon site C_f , to give an oxygen-containing active intermediate. The reaction between intermediate and either O_{ads} or gaseous O_2 produces CO/CO_2 [78]. The proposed mechanism implies the key role of surface adsorbed oxygen species (O_β) in soot oxidation, in contrast to CO oxidation via Mars and van Krevelen mechanism, which mainly involves O_α species. From the O 1s XP spectra of the samples it is clear that O_β peak of CM is most intense, which signifies presence of higher concentration of surface adsorbed oxygen species on CM surface. The O_β peak intensity of CF seems to be very low in the O 1s XP spectra (Fig. 6), which can be unambiguously correlated to the poor soot oxidation activity of CF (Fig. 10). Hence, we can conclude that amount of surface bound oxygen species controls the soot oxidation activity of doped ceria catalysts. However, which specific properties of the dopants control the concentration of surface bound oxygen species on doped ceria surface is not clear to our understanding. Hopefully, in our later investigations we will try to explore this matter of fact.

4. Conclusions

Nano-crystalline ceria solid solutions were successfully synthesized by incorporating Zr, Hf, La, Pr, Fe, and Mn metal ions via simple coprecipitation method. XRD, TEM and Raman spectroscopic investigation proved the formation of cubic fluorite phase ceria-based solid solution with perfect incorporation of the dopants. XPS examination was carried out to probe the surface properties, whereas, H_2 -TPR study provided the reducibility of the samples. The redox catalytic activities were investigated by means of CO and soot oxidation reactions, which are two important roles of ceria-based automotive catalysts. CM has been found to exhibit highest catalytic activity in both the processes. However, the order of activity followed by the other materials is different for CO and soot oxidation. Involvement of different mechanism and different oxygen species in both the processes would justify this variation in reactivity order. However, to find out the factors responsible for higher CO oxidation catalytic activity of CM, the physicochemical properties have been investigated with care and reasonably compared with those of other materials. Careful observation and reasonable justifications revealed the following facts: firstly, O 1s XPS of CM revealed a remarkable low binding energy for lattice oxygen, which may be attributed to the disparity of electronegativity of host and dopant ions. The loosely bound lattice oxygen promoted the CO oxidation activity of CM. In addition, higher degree of lattice strain in CM helped in maintaining better flow of oxygen from bulk to surface. Secondly, higher concentration of oxygen vacancies and Ce^{3+} ions on CM surface enhanced the redox property of ceria. Furthermore, Mn XPS indicated the presence of multiple oxidation of Mn ion in CM. Hence, presence of synergistic interaction between Ce and Mn redox couples can be justifiably predicted, which would promote the CO oxidation activity. On the other hand,

considerable low temperature soot oxidation activity of CM can be attributed to the higher concentration of surface adsorbed O species compared to other materials. Therefore, we conclude that all these factors demonstrated above together promote the physicochemical properties of manganese doped ceria towards enhanced catalytic activity for CO and soot oxidation.

Acknowledgement

DM and BG thank the Council of Scientific and Industrial Research (CSIR) and University Grant Commission (UGC) New Delhi for junior research fellowships. Financial support for this project was received from Department of Science and Technology, New Delhi, under SERB Scheme (SB/S1/PC-106/2012).

Appendix A. Supplementary data

Supplementary data associated with this article can be found, in the online version, at <http://dx.doi.org/10.1016/j.apcatb.2016.03.042>.

References

- [1] A. Trovarelli, *Catal. Rev. - Sci. Eng.* 38 (1996) 439–520.
- [2] A. Trovarelli, P. Fornasiero, *Catalysis by ceria and related materials Catalytic Science Series*, vol. 12, Imperial College Press, UK, 2013.
- [3] N.V. Skorodumova, S.I. Simak, B.I. Lundqvist, I.A. Abrikosov, B. Johansson, *Phys. Rev. Lett.* 89 (2002) 166601–1–166601–4.
- [4] I.I. Soykal, H. Sohn, U.S. Ozkan, *ACS Catal.* 2 (2012) 2335–2348.
- [5] J. Kašpar, P. Fornasiero, M. Graziani, *Catal. Today* 50 (1999) 285–298.
- [6] Q. Wanga, G. Li, B. Zhao, R. Zhou, *Appl. Catal. B* 100 (2010) 516–528.
- [7] S. Putla, M.H. Amin, B.M. Reddy, A. Nafady, K.A. Al Farhan, S.K. Bhargava, *ACS Appl. Mater. Interfaces* 7 (2015) 16525–16535.
- [8] P.W. Dunne, A.M. Carnerup, A. Wegrzyn, S. Witkowski, R.I. Walton, *J. Phys. Chem. C* 116 (2012) 13435–13445.
- [9] X. Tang, Y. Li, X. Huang, Y. Xu, H. Zhu, J. Wang, W. Shen, *Appl. Catal. B* 62 (2006) 265–273.
- [10] P. Venkataswamy, K.N. Rao, D. Jampaiah, B.M. Reddy, *Appl. Catal. B* 162 (2015) 122–132.
- [11] M. Nolan, *J. Phys. Chem. C* 115 (2011) 6671–6681.
- [12] Z. Hu, H. Metiu, *J. Phys. Chem. C* 115 (2011) 17898–17909.
- [13] D.A. Andersson, S.I. Simak, N.V. Skorodumova, I.A. Abrikosov, B. Johansson, *Appl. Phys. Lett.* 90 (2007) 031909–1–031909–3.
- [14] Y. Liu, C. Wen, Y. Guo, G. Lu, Y. Wang, *J. Phys. Chem. C* 114 (2010) 9889–9897.
- [15] C. Sun, D. Xue, *Phys. Chem. Chem. Phys.* 15 (2013) 14414–14419.
- [16] F. Yang, J. Graciani, J. Evans, P. Liu, J. Hrbek, J.F. Sanz, J.A. Rodriguez, *J. Am. Chem. Soc.* 133 (2011) 3444–3451.
- [17] P. Larsson, A. Andersson, *J. Catal.* 179 (1998) 72–89.
- [18] B.M. Reddy, K.N. Rao, P. Bharali, *Ind. Eng. Chem. Res.* 48 (2009) 8466–8478.
- [19] T. Andana, M. Piumetti, S. Bensaid, N. Russo, D. Fino, R. Pirone, *Appl. Catal. B* (2015), <http://dx.doi.org/10.1016/j.apcatb.2015.12.030>.
- [20] L. Katta, P. Sudarsanam, G. Thrimurthulu, B.M. Reddy, *Appl. Catal. B* 101 (2010) 101–108.
- [21] Q. Shen, M. Wu, H. Wang, C. He, Z. Hao, W. Wei, *Catal. Sci. Technol.* 5 (2015) 1941–1952.
- [22] J. Zhang, M. Gong, Y. Cao, C.-A. Wang, *RSC Adv.* 5 (2015) 95133.
- [23] X. Li, C. Ni, X. Lu, S. Zuo, W. Liu, C. Yao, *Catal. Sci. Technol.* 6 (2016) 545–554.
- [24] M. Piumetti, S. Bensaid, N. Russo, D. Fino, *Appl. Catal. B* 165 (2015) 742–751.
- [25] W. Gao, Z. Zhang, J. Li, Y. Ma, Y. Qu, *Nanoscale* 7 (2015) 11686–11691.
- [26] W. Liu, W. Wang, K. Tang, J. Guo, Y. Ren, S. Wang, *Catal. Sci. Technol.*, 10.1039/c5cy01241d.
- [27] Z. Ying, X. Chenjun, S. Yeqing, Z. Qiuliang, C. Yinfei, L. Hanfeng, *RSC Adv.* 5 (2015) 91734–91741.
- [28] V. D. Sarli, G. Landi, L. Lisi, A. Saliva, A. D. Benedetto, *Appl. Catal. B.*, 10.1016/j.apcatb.2016.01.073.
- [29] B.M. Reddy, G. Thrimurthulu, L. Katta, Y. Yamada, S.-E. Park, *J. Phys. Chem. C* 113 (2009) 15882–15890.
- [30] B.M. Reddy, P. Bharali, P. Saikia, A. Khan, S. Lorient, M. Muhler, W. Grunert, *J. Phys. Chem. C* 111 (2007) 1878–1881.
- [31] P. Sudarsanam, B. Mallesham, P.S. Reddy, D. Großmann, W. Grunert, B.M. Reddy, *Appl. Catal. B* 144 (2014) 900–908.
- [32] W.-J. Hong, S. Iwamoto, S. Hosokawa, K. Wada, H. Kanai, M. Inoue, *J. Catal.* 277 (2011) 208–216.
- [33] D. Valechha, S. Lokhande, M. Klementova, J. Subrt, S. Rayalu, J. Mater. Chem. 21 (2011) 3718–3725.
- [34] B.M. Reddy, A. Khan, *Catal. Surv. Asia* 9 (2005) 155–171.
- [35] G. Thrimurthulu, K.N. Rao, D. Devaiah, B.M. Reddy, *Res. Chem. Intermed.* 38 (2012) 1847–1855.
- [36] E. Aneggi, V. Cabbai, A. Trovarelli, D. Goi, *International Journal of Photoenergy*, 10.1155/2012/694721.
- [37] M. Castellanos, A.R. West, *J.C.S. Faraday I* 76 (1980) 2159–2169.
- [38] B. Choudhury, A. Choudhury, *Mater. Chem. Phys.* 131 (2012) 666–671.
- [39] P. Dutta, S. Pal, M.S. Seehra, Y. Shi, E.M. Eyring, R.D. Ernst, *Chem. Mater.* 18 (2006) 5144.
- [40] M.J.D. Rushton, A. Chroneos, *Sci. Rep.* (2014), <http://dx.doi.org/10.1038/srep06068>.
- [41] L. Xuesong, L. Jiqing, Q. Kun, H. Weixin, L. Mengfei, *J. Rare Earths* 27 (2009) 418–424.
- [42] V.G. Keramidas, W.B. White, *J. Chem. Phys.* 59 (1973) 1561–1562.
- [43] W.H. Weber, K.C. Hass, J.R. McBride, *Phys. Rev. B* 48 (1993) 178–185.
- [44] G. Gouade, P. Colomban, *Prog. Cryst. Growth Charact. Mater.* 53 (2007) 1–56.
- [45] S. Ramana, B. Govinda Rao, P. Venkataswamy, A. Rangaswamy, *J. Mol. Catal. A: Chem.* 415 (2016) 113–121.
- [46] D.W. Wheeler, I. Khan, *Vib. Spectrosc.* 70 (2014) 200–206.
- [47] B. Govinda Rao, P. Sudarsanam, A. Rangaswamy, B.M. Reddy, *Catal. Lett.* 145 (2015) 1436–1445.
- [48] B.M. Reddy, P. Bharali, T. Gode, P. Saikia, L. Katta, S.-E. Park, *Catal. Lett.* 123 (2008) 327–333.
- [49] A. Martinez-Arias, M. Fernandez-Garcia, L.N. Salamanca, R.X. Valenzuela, J.C. Conesa, J. Soria, *J. Phys. Chem. B* 104 (2000) 4038–4046.
- [50] W.Y. Hernandez, M.A. Centeno, F. Romero-Sarria, J.A. Odriozola, *J. Phys. Chem. C* 113 (2009) 5629–5635.
- [51] P. Sudarsanam, B. Hillary, D.K. Deepa, M. Hassan Amin, B. Mallesham, B.M. Reddy, S.K. Bhargava, *Catal. Sci. Technol.* 5 (2015) 3496–3500.
- [52] P. Venkataswamy, D. Jampaiah, F. Lin, I. Alkneit, B.M. Reddy, *Appl. Surf. Sci.* 349 (2015) 299–309.
- [53] E. Aneggi, C. d. Leitenburg, A. Trovarelli, *Catal. Today* 181 (2012) 108–115.
- [54] P. Venkataswamy, D. Jampaiah, K.N. Rao, B.M. Reddy, *Appl. Catal. A* 488 (2014) 1–10.
- [55] L. Liu, J. Tang, Y. Li, M. Guo, M. Zhang, X. Wang, *J. Nanosci. Nanotechnol.* 7 (2007) 2883–2888.
- [56] W.-T. Chen, K.-B. Chen, M.-F. Wang, S.-F. Weng, C.-S. Lee, M.C. Lina, *Chem. Commun.* 46 (2010) 3286–3288.
- [57] J.E. Fallah, S. Boujana, H. Dexpert, A. Kiennemann, J. Majerus, O. Touret, F. Villain, F.L. Normand, *J. Phys. Chem.* 98 (1994) 5522–5533.
- [58] S. Bernal, J.J. Calvino, G.A. Cifredo, J.M. Rodriguez-Izquierdo, *J. Phys. Chem.* 99 (1995) 11794–11796.
- [59] E. Aneggi, M. Boaro, C. de Leitenburg, G. Dolcetti, A. Trovarelli, *J. Alloys Compd.* 408–412 (2006) 1096–1102.
- [60] X. Tang, Y. Li, X. Huang, Y. Xu, H. Zhu, J. Wang, W. Shen, *Appl. Catal. B* 62 (2006) 265–273.
- [61] S. Royer, D. Duprez, *ChemCatChem* 3 (2011) 24–65.
- [62] S.B. Simonsen, S. Dahl, E. Johnson, S. Helveg, *J. Catal.* 255 (2008) 1–5.
- [63] P. Bharali, P. Saikia, L. Katta, B.M. Reddy, *J. Ind. Eng. Chem.* 19 (2013) 327–336.
- [64] M. Huang, S. Fabris, *J. Phys. Chem. C* 112 (2008) 8643–8648.
- [65] C.T. Campbell, C.H.F. Peden, *Science* 309 (2005) 713–714.
- [66] M.W. Zhao, M.Q. Shen, J. Wang, *J. Catal.* 248 (2007) 258–267.
- [67] C. Binet, A. Badri, M. Boutonnet-Kizling, J.C. Lavalley, *J. Chem. Soc. Faraday Trans.* 90 (1994) 1023.
- [68] F. Bozon-Verduraz, A. Bensalem, *J. Chem. Soc. Faraday Trans.* 90 (1994) 653.
- [69] C.-W. Tang, L.-C. Hsu, S.-W. Yub, C.-B. Wang, S.-H. Chien, *Vib. Spectrosc.* 65 (2013) 110–115.
- [70] M.F. Wilkes, P. Hayden, A.K. Bhattacharya, *J. Catal.* 219 (2013) 295–304.
- [71] Y. Liu, C. Wen, Y. Guo, G. Lu, Y. Wang, *J. Mol. Catal. A: Chem.* 316 (2010) 59–64.
- [72] E.S. Putna, B. Shereck, R.J. Gorte, *Appl. Catal. B* 17 (1998) 101–106.
- [73] T. Bunluesin, R.J. Gorte, G.W. Graham, *Appl. Catal. B* 14 (1997) 105–115.
- [74] Y. Zhao, B.-T. Teng, X.-D. Wen, Y. Zhao, Q.-P. Chen, L.-H. Zhao, M.-F. Luo, *J. Phys. Chem. C* 116 (30) (2012) 15986–15991.
- [75] H.Y. Kim, H.M. Lee, G. Henkelman, *J. Am. Chem. Soc.* 134 (2012) 1560–1570.
- [76] W. Song, A.P. Jansen, E.J. Hensen, *Faraday Discuss.* 162 (2013) 281–292.
- [77] E. Aneggi, C. de Leitenburg, G. Dolcetti, A. Trovarelli, *Catal. Today* 114 (2006) 40–47.
- [78] W.F. Shangguan, Y. Teraoka, S. Kagawa, *Appl. Catal. B* 12 (1997) 237–247.